The El Niño–Southern Oscillation in the Second Hadley Centre Coupled Model and Its Response to Greenhouse Warming

MATTHEW COLLINS

Hadley Centre for Climate Prediction and Research, Meteorological Office, Bracknell, United Kingdom

(Manuscript received 19 March 1999, in final form 14 June 1999)

ABSTRACT

This paper describes El Niño–Southern Oscillation (ENSO) interannual variability simulated in the second Hadley Centre coupled model under ''control'' and ''greenhouse warming'' scenarios. The model produces a very reasonable simulation of ENSO in the control experiment—reproducing the amplitude, spectral characteristics, and phase locking to the annual cycle that are observed in nature. The mechanism for the model ENSO is shown to be a mixed SST–ocean dynamics mode that can be interpreted in terms of the ''ocean recharge paradigm'' of Jin.

In experiments with increased levels of greenhouse gases, no statistically significant changes in ENSO are seen until these levels approach four times preindustrial values. In these experiments, the model ENSO has an approximately 20% larger amplitude, a frequency that is approximately double that of the current ENSO (implying more frequent El Niños and La Niñas), and phase locks to the annual cycle at a different time of year. It is shown that the increase in the vertical gradient of temperature in the thermocline region, associated with the model's response to increased greenhouse gases, is responsible for the increase in the amplitude of ENSO, while the increase in meridional temperature gradients on either side of the equator, again associated with the models response to increasing greenhouse gases, is responsible for the increased frequency of ENSO events.

1. Introduction

The El Niño–Southern Oscillation [ENSO; see, e.g., Philander (1990)] is the largest mode of interannual variability of the global climate system. It arises from a dynamical interaction of the ocean and atmosphere in the equatorial Pacific and it impacts the weather and climate both locally and via teleconnections to remote areas. In this study we examine the interannual ENSO-like variability in the second Hadley Centre coupled climate model (HadCM2). The goals of the study are twofold. First, we wish to assess how well HadCM2 simulates the ENSO phenomenon, and second we wish to see if ENSO changes in the model when we increase the levels of greenhouse gases and other radiatively important anthropogenic substances.

The ability of global coupled climate models to simulate the ENSO phenomenon has, to date, been rather limited. Many models simulate some variability in the tropical Pacific but this is usually too weak (Tett 1995; Knutson et al. 1997; Meehl and Arblaster 1998; Timmermann et al. 1999a), although some models are beginning to show a better simulation (Bacher et al. 1998) and it is suggested that some do, at least, capture the essential physics of the mode (Timmermann et al. 1999a). Failure to simulate ENSO leads to an underestimation of the global interannual variability. This undermines confidence in coupled models and can have important implications for the detection of climate change as the techniques employed rely crucially on an estimate of the ''internal'' variability of the system (Hasselmann 1993). Also, a realistic fully coupled model simulation of ENSO will lead to better understanding of the phenomenon to complement much of the current understanding, which is based on analysis of observations and of ''reduced physics'' models (see, e.g., Neelin et al. 1998).

The effect of current increased levels of greenhouse gases on ENSO has been a controversial issue of late. The El Niños of 1982/83 and 1997/98 were the biggest on record if one measures their amplitude by the size of the Niño-3 anomaly. The basic problem is one of assessing changes in, what is essentially, a very short and noisy time series. Trenberth and Hoar (1996) suggest that the trend of more frequent ENSO events since 1976, and the excessive central Pacific warm anomalies during the first half of the 1990s, are unlikely when compared to the past observational record. However, Rajagopalan et al. (1997) show that this result is sensitive to the statistical model used in the calculation (see

Corresponding author address: Dr. Matthew Collins, Hadley Centre for Climate Prediction and Research, Meteorological Office, London Road, Bracknell, RG12 2SZ, United Kingdom.
E-mail: matcollins@meto.gov.uk

also Wunsch 1999). In a recent study, Timmermann (1999) uses an optimal fingerprinting technique (e.g., Hasselmann 1993) to show that the current ENSO behavior is not unusual, although the outcome of this type of study is rather dependent on having an accurate simulation of the natural variability of ENSO.

It is useful to consider the effect of increasing greenhouse gases in the tropical Pacific in two ways. First, together with changes in the global temperature of the ocean, there exists the possibility of a regional pattern of SST change such that the east warms more rapidly than the west giving an El Niño–like pattern of change (e.g., Meehl and Washington 1996; Knutson and Manabe 1998) or where the west warms more rapidly than the east giving a La Niña–like change (Cane et al. 1997). Superimposed on such changes in the mean climate, there also exists the possibility of changes in the statistics (e.g., the amplitude and timescale) of ENSO (e.g., Timmermann et al. 1999b). In this paper we mainly concentrate on the latter effect; however, it must be noted that the impacts of any changes in ENSO statistics, for example modifications to the drought/flood cycle, will be affected by changes in the mean climate and may well interact with them in a nontrivial way.

Assessment of the response of ENSO statistics to future increases of greenhouse gases in climate models initially showed very little or no change as levels increased (Tett 1995; Knutson et al. 1997; Meehl et al. 1993). However these models suffered from rather poor simulations of ENSO for present-day conditions. More recently models have improved and Timmermann et al. (1999b) claim to see significant increases in the amplitude of ENSO and in the distribution of events with La Niñas becoming more frequent than El Niños toward the end of the twenty-first century under the Intergovernmental Panel on Climate Change's (IPCC) IS92a scenario (Houghton et al. 1995) emissions. Such changes would have profound consequences for the global climate and subsequently on the lives of many people. Therefore it is important to assess if such changes are consistently found in other models.

Section 2 briefly describes HadCM2, the coupled model used in this study. Section 3 describes the characteristics of the ENSO signal computed from the control run of HadCM2. Section 4 describes the changes in the simulated ENSO signal when levels of greenhouse gases are increased in the model. Section 5 describes the mechanisms responsible for the ENSO variability in the model and section 6 describes why the ENSO changes in the model in terms of the mechanisms proposed. Finally, the results are summarized and conclusions are draw in section 7.

2. HadCM2: The second Hadley Centre Coupled Model

For a full description of the formulation, mean climate, and variability of HadCM2 the reader is referred to Johns et al. (1997) and Tett et al. (1997). Briefly, the atmosphere model is based on that currently in use at the U.K. Meteorological Office for numerical weather prediction (Cullen 1993) and the ocean model is based on the Bryan–Cox primitive equation model (Cox 1984). Both the ocean and the atmosphere model are solved on a 2.5° lat × 3.75° long grid with the atmosphere model having 19 levels in the vertical and the ocean model having 20 levels. The models are coupled using a seasonally varying flux correction of temperature and salinity in order to keep the model climate from drifting. The flux correction term has a seasonal cycle and is based on the climatology of Levitus (1982) and is fixed for the duration of the control and all the scenario runs (see Johns et al. 1997 for more details). The radiative effects of greenhouse gases are parameterized by ''equivalent CO_2'' and the effects of sulfate aerosols are parameterized by modifying the surface albedo (Mitchell and Johns 1997).

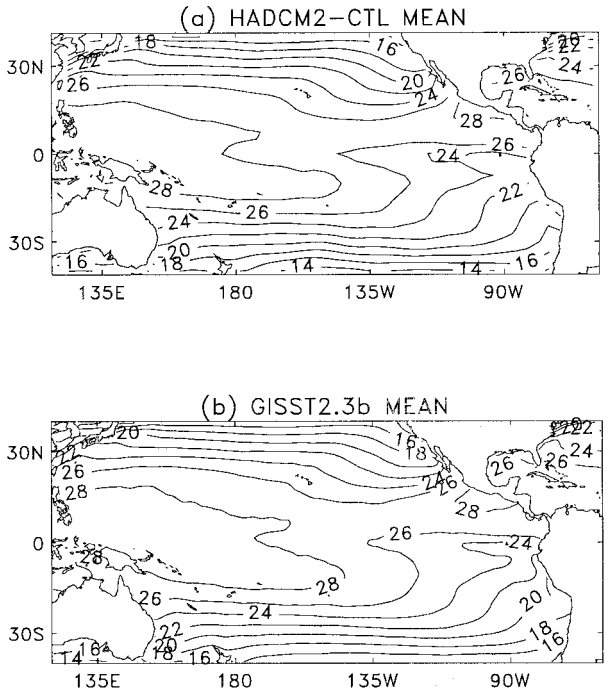

FIG. 1. Sea surface temperatures for the Pacific region from (a) the HadCM2 control integration and (b) from the GISST 2.3b observations.

3. ENSO in the HadCM2 control integration

Although the mean climate of the HadCM2 control and its variability are documented in previous papers (Johns et al. 1997; Tett et al. 1997), we show the main features of the tropical Pacific climate of the model here to set the scene before the more detailed analysis is presented. Figures 1 and 2 show the mean and the standard deviation of the sea surface temperatures (SSTs) in the Pacific region from the model and from the Global

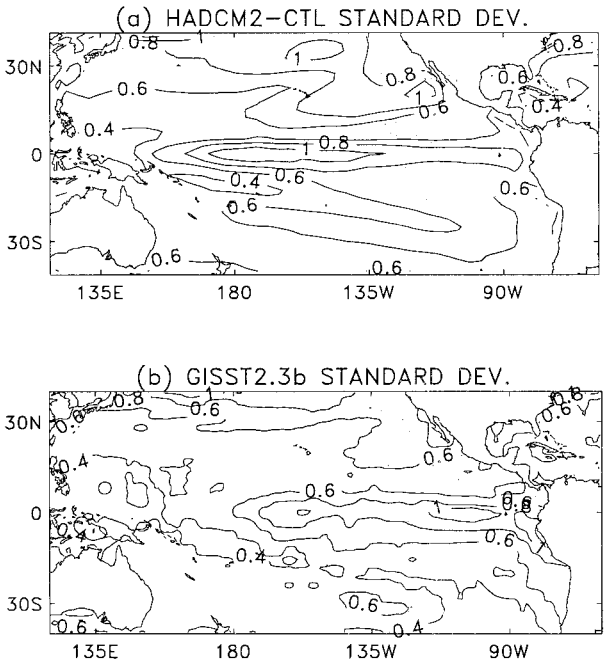

FIG. 2. The interannual standard deviations of sea surface temperatures for the Pacific region from (a) the HadCM2 control integration and (b) from the GISST 2.3b observations.

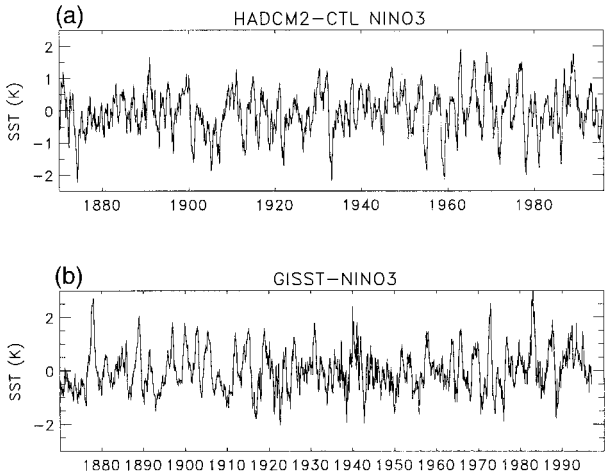

FIG. 3. SST anomalies averaged in the Niño-3 region (5°N–5°S, 150°W–90°W) from a subsection of the (a) HadCM2 control and from the (b) GISST 2.3b observations. In each case values are computed from monthly means and the mean seasonal cycle is removed. Years marked on the abscissa for the control run (a) are essentially arbitrary although the run uses 1850 as its start year.

Ice and Sea Surface Temperature (GISST) observations of Rayner et al. (1996). The mean SSTs are simulated very well by the model with the warm pool in the west and the cold tongue in the east. This agreement is, in part, due to the flux correction term, which alleviates many of the errors that seem to be inherent in the mean climates of coupled models (e.g., Neelin et al. 1992; Kiehl 1998). The standard deviation of the observed SSTs (Fig. 2b) shows maxima of variability in the east on the equator and off the coast of South America. The corresponding model plot (Fig. 2a) shows a single maxima in the central Pacific with the variability extending too far west in comparison with the observations [an error that is typical of many coupled models, e.g., Meehl and Arblaster (1998)]. Also the model simulates too much variability off the coast of California. Nevertheless, close to the equator, the model produces ENSO-like variability with about the right magnitude.

We next make use of a common index for ENSO, namely the Niño-3 index, which is defined as the SST anomalies averaged in the region 5°N–5°S, 90°W–150°W. A 130-yr segment of the Niño-3 index computed from the 1700 yr of the HadCM2 control is shown in Fig. 3. Also show is the Niño-3 index computed from the GISST observations. A quick inspection of the two series reveals that the model captures the amplitude of the Niño-3 index well. Indeed, the standard deviation of the entire 1700-yr model series is 0.74 while that of the observed series is 0.78. We choose to use the Niño-3 index as a measure of ENSO thoughout the paper as it is a commonly used index that aids comparison with the observations and with other published work. Because of the tendency of the model to overestimate interannual variability in the central Pacific (Fig. 2) we could have taken, for example, the Niño-4 region (5°N–5°S, 160°E–150°W). However, there is little difference in the main results of the paper when looking at either index as they are highly correlated in the model (coefficients are 0.73 for monthly anomalies and 0.87 for annual anomalies) and respond in the same way to increases in greenhouse gases.

We next compare the frequency characteristics of the model control Niño-3 index and the observed Niño-3 index. To compute spectra we take the Fourier transform of the autocovariance function of the time series and apply the Tukey–Hanning window to get a consistent and unbiased estimate of the power spectrum (Chatfield 1984). A window width of 13 yr was chosen and the mean annual cycle was removed from all time series before processing. The power spectrum of the GISST Niño-3 index computed using this method is shown by the thick black line in Fig. 4. The familiar peak in the spectrum at periods of 2–8 yr is evident indicating the

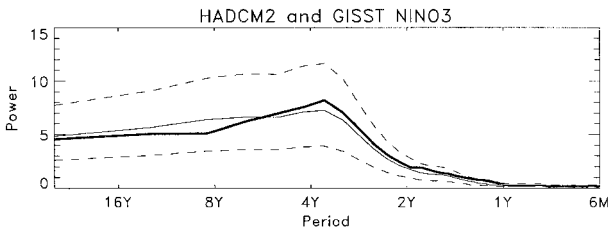

FIG. 4. Power spectra of the GISST 2.3b Niño-3 index (thick black line) and the HadCM2 control Niño-3 index (thin black line). The thin dashed lines indicate the 95% interval for the power spectra from the control.

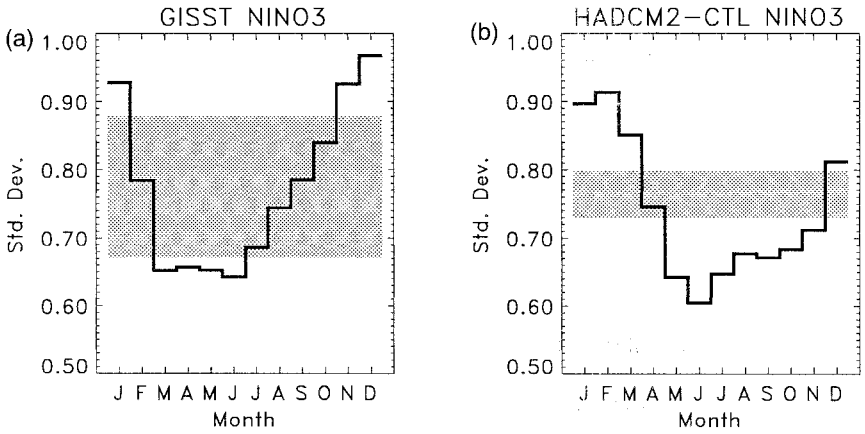

FIG. 5. Standard devations of the Niño-3 anomaly partitioned by month for (a) the GISST observations and for (b) the HadCM2 control run. Values outside the gray-shaded area are significant at the 5% level based on a null hypothesis of AR(1) noise.

cyclic nature of ENSO. Note that there is no split in the spectrum with peaks at 2 and 4 yr as was found by other authors (Jiang et al. 1995).

Also shown as the thin black line in Fig. 4 is the power spectrum of the long model control Niño-3 index, together with an estimate of the variability of this quantity shown by the thin dashed lines. This estimate of the variability is simply the 95% confidence interval based on the χ^2 distribution. Similar estimates of the variability have been computed by taking overlapping segments of the control run and finding the maximum and minimum power in each spectral bin (e.g., Gillett et al. 2000) and similar confidence intervals are found. The model spectra in Fig. 4 show a peak in the 2–8 yr band, remarkably similar to that in the observations and, moreover, the observations lie within the variability of the computed model spectra, indicating that the model reproduces the main frequency characteristics of the Niño-3 index.

While power spectra show information about the *global* frequency characteristics, information about the *local* characteristics can be found by computing the wavelet power spectrum (e.g., Torrence and Compo 1998). The wavelet power spectrum of the HadCM2 control Niño-3 shows similar features to that of the observed Niño-3 index (figure not shown), indicating that, not only does the model reproduce the main frequency characteristics of the Niño-3 index well, but it also reproduces the temporal modulation of the index with an indication of ''breaks'' and ''active phases'' of ENSO.

A well-known feature of ENSO is its phase locking to the annual cycle. ENSO events peak most frequently during the northern winter months (giving the name El Niño) and it is desirable that any model of ENSO captures this phase locking. It has also been suggested (Jin et al. 1994; Tziperman et al. 1994) that the annual cycle may be an integral part of the dynamics of ENSO and may be responsible for the irregular nature of the cycle. Figure 5 shows the standard deviation of the Niño-3 index partitioned by month for the GISST observations and for the HadCM2 control. For the observations the maximum standard deviations occur in the northern winter months while the minimum standard deviations occur during the northern early spring and summer months. For HadCM2 there is a similar picture with comparable variance spread across the months, albeit with the curve slightly lagging the observations by a month or two.

4. ENSO response to increases in greenhouse gases

A large array of HadCM2 experiments have been performed in which levels of (equivalent) CO_2 increase according to various scenarios and the main results have been published in a series of papers (e.g., Mitchell et al. 1995; Tett et al. 1996; Hegerl et al. 1997; Mitchell and Johns 1997). In this study we have analyzed the following experiments to see if the ENSO behavior found in the control integration changes in response to such increases.

- G ensemble: This is an ensemble of four integrations starting at 1860 and using the observed historic equivalent CO_2 forcing up to the present day and then the IPCC IS92a (Houghton et al. 1995) scenario up to 2100. The different initial conditions for the ensemble were taken from the control run at 150-yr intervals.
- GS ensemble: The same as the G ensemble but with the effects of sulfate aerosols parameterized by the modification of the surface albedo field (Mitchell and Johns 1997).
- $2\times CO_2$: A double CO_2 equilibrium experiment started from the time of double CO_2 from a run with a 1% yr^{-1} CO_2 increase; 180 yr of the run were used in the analysis.
- $4\times CO_2$: A quadruple CO_2 equilibrium experiment started from the time of quadrupled CO_2 from the first

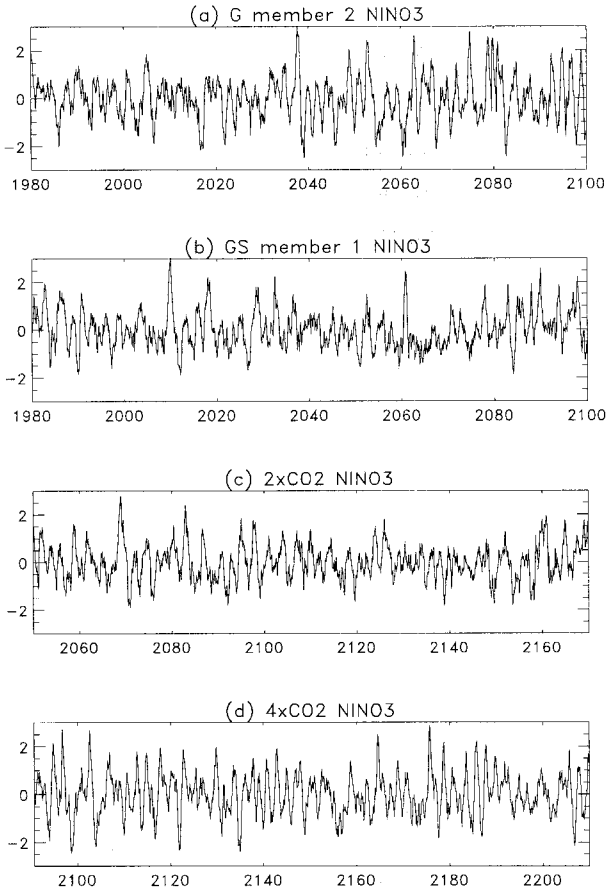

FIG. 6. Time series of the Niño-3 index from (a) G ensemble member 1, (b) GS ensemble member 1, (c) the $2\times CO_2$ experiment, and (d) the $4\times CO_2$ experiment.

member of the G ensemble; 180 yr of the run were used in the analysis.

We are interested in changes in the amplitude of ENSO, changes in the spectral characteristics, and changes in the phase locking to the annual cycle with respect to the control integration. Time series of the Niño-3 index are shown in Fig. 6 from member 2 of the G ensemble, and from member 1 of the GS ensemble, from the $2\times CO_2$ and from the $4\times CO_2$ experiments. Linear trends have been removed from the all the series using linear regression. On comparison with the control and observed series (Fig. 3), it can be seen by eye that the amplitude of the oscillations in the Niño-3 index increases toward the end of the G ensemble member and in the $4\times CO_2$ experiment whereas no such increase is evident in the GS or $2\times CO_2$ run. Standard deviations of the Niño-3 index for all the experiments, and for the observations, are shown in Table 1. Bold numbers indicate standard deviations that exceed the standard deviation of the HadCM2 control Niño-3 index at the 95% level. There is a general trend of increasing standard deviations in the G ensemble but there is no corresponding increase in the GS ensemble (although ensemble member 2 does have a significantly larger standard deviation in the 2070–2100 time period). For the equilibrium experiments there is no change compared to the control at $2\times CO_2$ but there is a significant increase in the standard deviation of approximately 20% at $4\times CO_2$.

We have shown then that the amplitude of ENSO increases toward the end of the twenty-first century in some of the transient runs and that it increases quite markedly in the $4\times CO_2$ experiment. Next, we examine the frequency characteristics of the Niño-3 index from all the runs and compare these with the ''envelope'' of variability from the control run (see Fig. 4). Recall that the control NINO3 index showed a peak in the 2–8-yr period band in good agreement with the observations.

Figure 7 shows the power spectra of the G ensemble, the GS ensemble, and the $2\times CO_2$ and $4\times CO_2$ equilibrium experiments. The spectra from the G and GS ensembles were computed using the Niño-3 index from years 2000 to 2100 and the spectra from the equilibrium experiments were computed from the first 100 yr of the

TABLE 1. Standard deviations of the Niño-3 index taken from the observations (GISST), the HadCM2 control run (CTL), from runs with increasing levels of greenhouse gases (G), and increasing greenhouse gases and sulfate aerosols (GS) and from the double and quadruple CO_2 runs. Four-digit numbers indicate years and standard deviations in bold indicate statistically significant departures from the control run at the 95% levels.

HADCM2-CTL	0.74	GISST	0.78
G member 1 2000–30	0.71	G member 2 2000–30	0.78
G member 3 2000–30	0.73	G member 4 2000–30	0.81
GS member 1 2000–30	0.84	GS member 2 2000–30	0.72
GS member 3 2000–30	0.78	GS member 4 2000–30	0.84
G member 1 2035–65	0.84	G member 2 2035–65	**1.08**
G member 3 2035–65	0.77	G member 4 2035–65	0.73
GS member 1 2035–65	0.69	GS member 2 2035–65	0.77
GS member 3 2035–65	0.79	GS member 4 2035–65	0.77
G member 1 2070–2100	0.90	G member 2 2070–2100	**1.03**
G member 3 2070–2100	0.78	G member 4 2070–2100	**1.04**
GS member 1 2070–2100	0.75	GS member 2 2070–2100	**0.95**
GS member 3 2070–2100	0.78	GS member 4 2070–2100	0.80
$2\times CO_2$	0.72	$4\times CO_2$	**0.91**

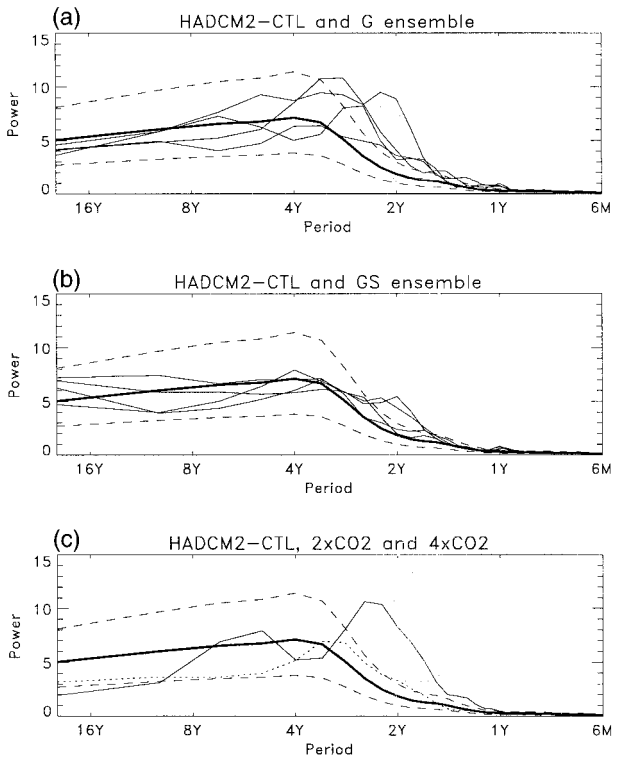

FIG. 7. Power spectra of Niño-3 index from (a) the G ensemble (thin solid lines), (b) the GS ensemble (thin solid lines), and for (c) the $2\times CO_2$ (dotted line) and $4\times CO_2$ (thin solid line) experiments. In each plot the power spectra of the HadCM2 control Niño-3 index is shown by the thick black line and its 95% interval is shown by the thin dashed lines.

respective runs. The thick black line in Fig. 7 shows the spectrum of the control and the 95% interval is indicated by the thin dashed lines (see section 3). Graphs of spectral power lying outside these lines indicate statistically significant departures from the control run and we can say that we have found a change in the frequency characteristics of ENSO. Significant departures can be seen in all of the G ensemble with anomalous peaks in the 1.5–3-yr band. Smaller, but significant, deviations are see in two of the GS members while the other two are indistinguishable from the control. Perhaps the most striking plot is that for the equilibrium experiments. The power spectrum of the $2\times CO_2$ Niño-3 index is, statistically, no different from the control whereas that for the $4\times CO_2$ experiment shows a marked increase in power in the 1.5–3-yr band and also a reduction of power at low frequencies. Indeed the high-frequency nature of ENSO is clearly apparent in Fig. 6 when compared with the corresponding series from the control run (Fig. 3), with an approximate doubling of the frequency in the $4\times CO_2$ case.

The phase-locking diagnostics (see section 3 and Fig. 5) for the $2\times CO_2$ and $4\times CO_2$ experiments are shown in Fig. 8. There is a small, but significant, change in the phase-locking characteristics in the $2\times CO_2$ case with the minimum standard deviations occurring in Northern Hemisphere spring rather than summer. However, the tendency for ENSOs to occur during the winter months remains the same. The largest changes occur in the $4\times CO_2$ experiment in which ENSOs occur more frequently in the late summer and autumn months compared to the winter phase locking in the control and in the observations. Such a change in the timing of ENSO events may have a large effect on the way ENSO has an impact on the local climate of the Tropics and on the teleconnection patterns, which transmits the signal of ENSO into the midlatitudes. Changes in the phase locking could be possibly linked to changes in the mean annual cycle in the east Pacific. HadCM2 has a seasonally varying flux correction term and thus simulates the mean annual cycle in the Pacific well in the control. There are no significant changes in the annual cycle at $4\times CO_2$ in comparison with the control (possibly because of the seasonally varying flux correction); thus,

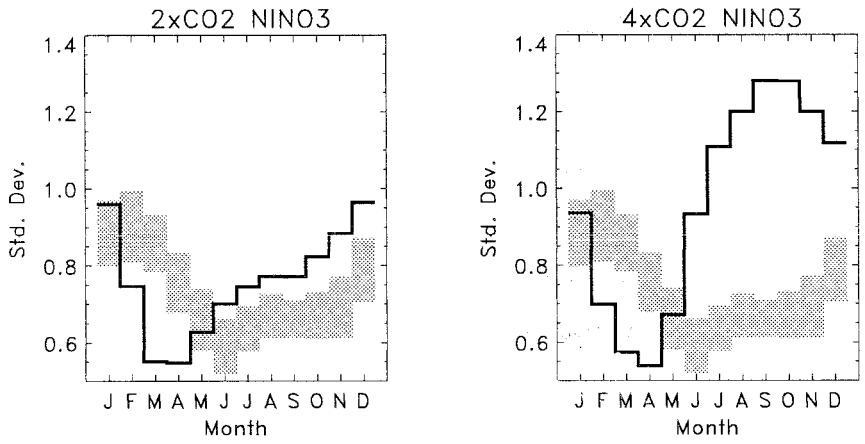

FIG. 8. Standard devations of the Niño-3 anomaly partitioned by month for the $2\times CO_2$ experiment (left panel) and for the $4\times CO_2$ experiment (right panel). Values outside the gray-shaded area are statistically different from the HadCM2 control run at the 5% level.

the mechanism for changing the timing of ENSO events with respect to the annual cycle appears to be more complicated.

To summarize, we may simply compare the ENSO signal from the control and the $4\times CO_2$ equilibrium experiment. The model ENSO response to increases in greenhouse gases is manifest as follows:

- A significant increase in the amplitude of ENSO of around 20%.
- An increase in the frequency of ENSO events with that increase concentrated in the 1.5–3-yr period band, a halving of the period of ENSO, indicating more frequent El Niño and La Niña events.
- A change in the phase locking of ENSO to the seasonal cycle, with events occurring more frequently in late northern summer/early autumn rather than during winter.

In order to understand these changes, we must first uncover the mechanisms that generate the control model ENSO.

5. Mechanisms for ENSO in HadCM2

In this section we identify the mechanism that generates the ENSO variability in the HadCM2 control run. Bjerknes (1969) was the first to propose a mechanism for ENSO in terms of a coupled ocean–atmosphere instability. In the Bjerknes hypothesis, positive SST anomalies in the eastern Pacific cause the trade winds to slacken thus reducing the equatorial upwelling via reduced Ekman transport. This leads to a positive feedback on the SST anomalies and the original anomaly is reinforced (and vice versa for cold anomalies). While this hypothesis can explain the phases of ENSO, it fails to explain the transitions between warm and cold events. This lead to the idea that subsurface ocean dynamics were of possible importance and the delayed-oscillator mechanism for ENSO was proposed (e.g., Suarez and Schopf 1988). In the delayed-oscillator model, a westerly wind anomaly in the central equatorial Pacific initiates a eastward propagating Kelvin wave and westward propagating Rossby wave. The Kelvin wave deepens the thermocline in the eastern Pacific leading to warm SST anomalies (El Niño), while the Rossby wave propagates to the western boundary and reflects as a Kelvin wave, which crosses the Pacific basin and elevates the thermocline in the east giving the cold phase (La Niña).

Both the Bjerknes coupled instability mode and the delayed-oscillator model seem plausible mechanisms for ENSO, with elements of both observed in nature and in ocean–atmosphere models of varying complexity. In a series of three papers, Jin and Neelin (1993), Neelin and Jin (1993a), Neelin and Jin (1993b) unified the two theories, representing them as limiting cases of the coupled problem. In the *fast-wave* limit, oceanic adjustment occurs quickly relative to SST timescales and unstable stationary or propagating SST modes are responsible for ENSO variability. This may be likened to the Bjerknes coupled instability mechanism. In the *fast-SST* limit, the timescales of SST adjustment are much faster than those of the subsurface ocean dynamics, which provide a ''memory'' for the system. Slow ocean modes thus control the ENSO variability, a situation that may be likened to the rather pathological case of having one Kelvin and one Rossby wave in the delayed-oscillator model. For realistic parameters of the coupled problem two limiting cases, the fast-wave and fast-SST limits, merge to form mixed SST–ocean dynamics modes or the ''subsurface memory paradigm'' (Neelin et al. (1998).

The existence of a mixed SST–ocean dynamics mode implies that there will be a part of the subsurface ocean that is in quasi-instantaneous balance with applied wind stress and a part that will be out of balance and that carries the ''memory'' of the ENSO cycle (quasi-instantaneous implying a timescale that is considerably shorther than the 2–8-yr ENSO cycle). Schneider et al. (1995) devised a clever set of experiments with an ocean-only model in which they forced the model with the observed wind stress to get a simulation of ENSO and then forced the model with the same wind stress but with the time direction reversed. They found that the *zonally asymmetric* heat content anomalies, corresponding to a seesaw motion of the thermocline, were very similar in the two experiments indicating that this part of the subsurface ocean was in equilibrium with the applied wind stress. However, the *zonally symmetric* heat content anomalies, corresponding to an up–down oscillation of the thermocline, were very different in the two experiments indicating that this part of the subsurface ocean provides the memory for ENSO.

An obvious way to assess the mechanisms for ENSO in HadCM2 would be to repeat the study of Schneider et al. (1995) using either the observed wind stress or some period of wind stress taken from the control run. This however involves uncoupling the ocean component from the atmosphere, which is unsatisfactory as we are looking for the ENSO mechanism in the fully coupled case. However, we may proceed by exploiting the fact that we have a long control run of 1700 yr. By searching backward and forward through the model history we might find a period in which the wind stress forcing forward in time is very similar to the wind stress forcing backward in time in another period. By comparing the ocean states from these two periods we can assess which part is in balance with the applied wind stress and which part is out of balance.

Indeed we can find two periods in the control when the wind stress forcing forward in time is reasonably similar to the wind stress forcing backward in time. Figure 9 shows the zonal wind stress averaged in the central Pacific (5°N–5°S, 165°E–135°W) for 20 yr from 1957 (solid line, the control run arbitrarily starts at 1850) and for 20 yr from 2496, plotted with the time axes reversed (dashed line). The data have been smoothed

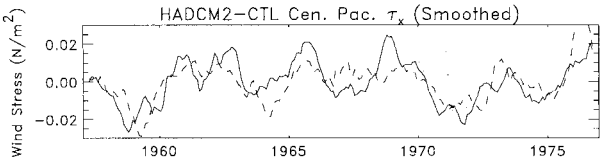

FIG. 9. Zonal wind stress anomalies from the HadCM2 control run averaged in the central Pacific (5°N–5°S, 165°E–135°W) for 20 yr from 1957 (solid line) and for 20 yr from 2496 plotted with the time axes reversed (dashed line). The data are smoothed with a 6-month running window to remove high-frequency noise.

with a 6-month running window to remove high-frequency noise. There is interannual variability in both series and, aside from a short period in the middle of diagram, there is a good agreement between the forward and backward curves. We denote these two periods as *forward* (control years 1957–76) and *backward* (control years 2515–2496).

Following Schneider et al. (1995) we now plot a longitude–time diagram of thermocline depth anomalies, averaged from 5°N to 5°S, for the forward and backward cases; see Fig. 10. Schneider et al. (1995) use vertically averaged temperature as a surrogate for thermocline depth; here we use the depth of the 20°C isotherm, denoted as *D*20. It would be easy to conclude from Fig. 10 that the propagating features in the thermocline depth are due to oceanic Rossby and Kelvin waves. However a closer examination of the phase speeds shows that these are incommesurate with the speeds of freely propagating waves, and moreover, the model used here has a very coarse resolution and could not represent these waves explicitly.

There is very little similarity between the *D*20 anom-

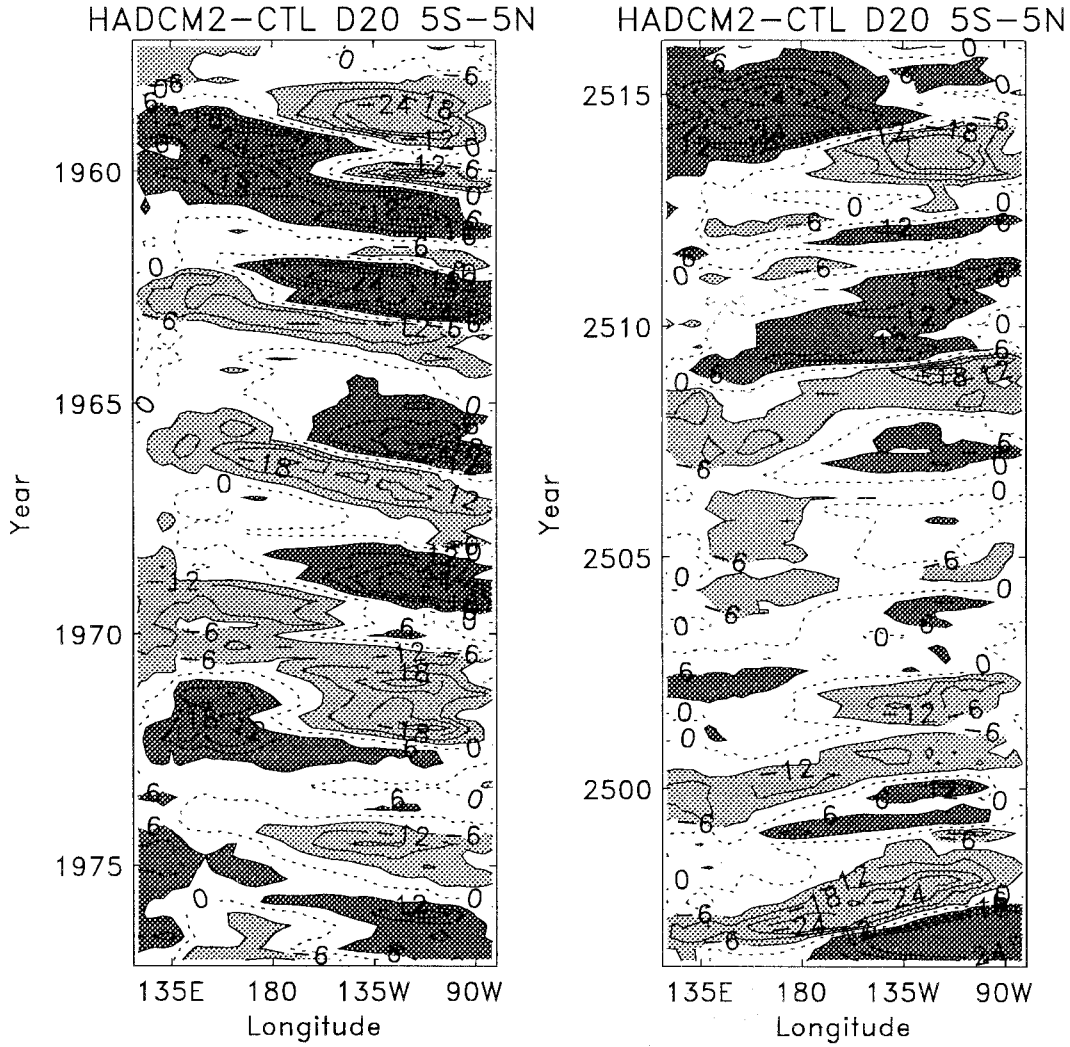

FIG. 10. Hovmöller diagrams of *D*20 (the depth of the 20°C isotherm) anomalies averaged from 5°S to 5°N for the forward and backward cases explained in the text. Note that time runs downward in the left diagram and upward in the right diagram.

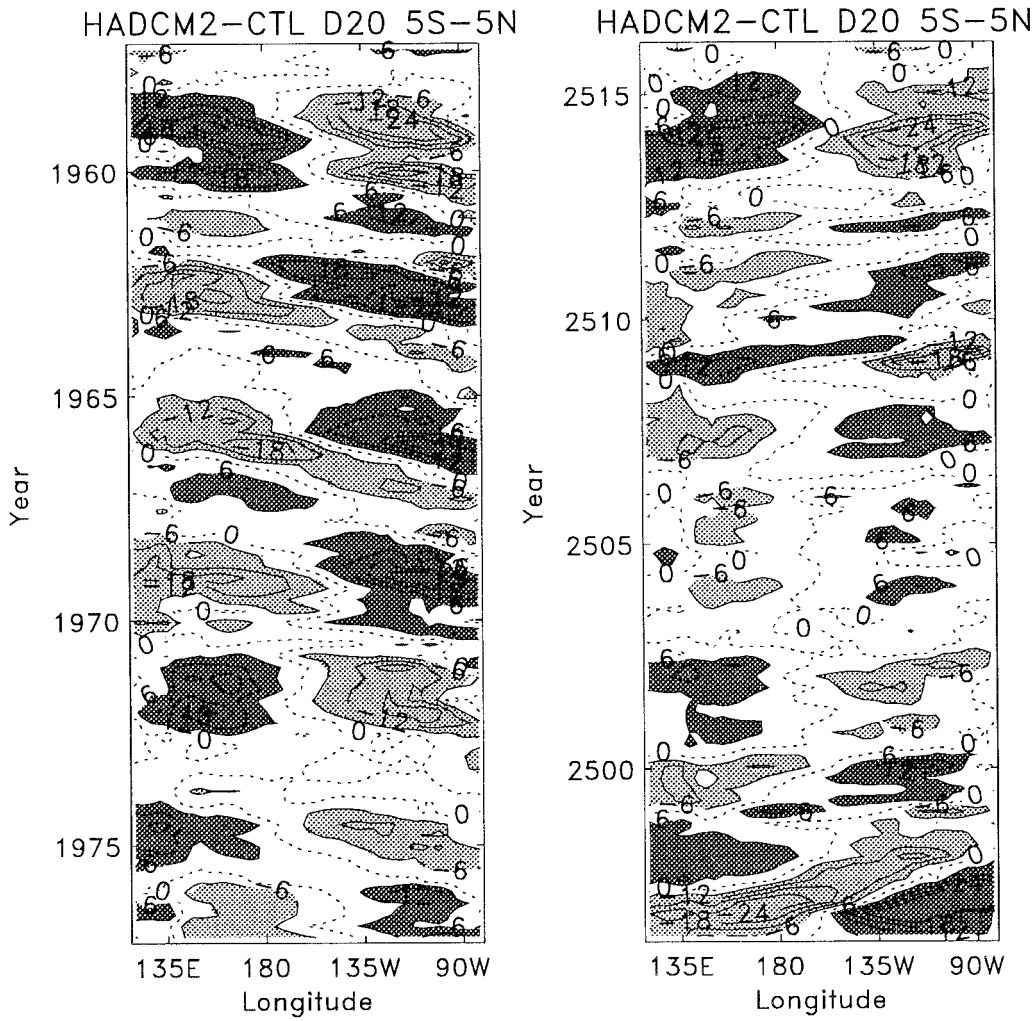

FIG. 11. Hovmöller diagrams of *D*20 (the depth of the 20°C isotherm) anomalies averaged from 5°S to 5°N, *and with the zonal mean removed*, for the forward and backward cases explained in the text. Note that time runs downward in the left diagram and upward in the right diagram.

alies in the forwards and backwards cases (the correlation coefficient between the fields is 0.2) and we might conclude that the subsurface ocean is far from equilibrium with the applied wind stress forcing implying that the model is close to the fast-SST limit. However, again following Schneider et al. (1995) we plot the same diagram but with the zonal mean removed (Fig. 11). We now see a qualitative agreement between the fields in comparison with the corresponding figure with the zonal mean included [see Figs. 6 and 7 of Schneider et al. (1995) for similar plots]. The agreement between the fields is not as good as that found by Schneider et al. (1995), with the correlation being 0.4 compared to correlations of 0.8 found by them. However, the correlations are certain to be lower as the forward and backward wind stress forcings are not exactly the same in this analysis. We conclude from this, and from examining other fields from the model, that at least part of the subsurface ocean, that is, the zonally asymmetric part or thermocline slope, is in approximate equilibrium with the instantaneous zonal wind stress. The zonally symmetric component, or mean thermocline depth, is not in balance with the instantaneous wind stress and carries the memory of ENSO. The Pacific wide zonal mean 20° isotherm depth anomalies, averaged from 5°N to 5°S, are shown in Fig. 12. The maximum correlation between these two time series occurs at a lag of 21

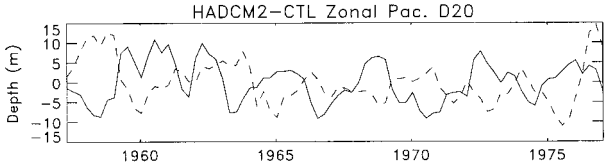

FIG. 12. The *D*20 anomalies from HadCM2-CTL averaged over the whole equatorial Pacific basin (5°N–5°S, 120°E–80°W) for 20 yr from 1957 (solid line) and for 20 yr from 2496 plotted with the time axes reversed (dashed line).

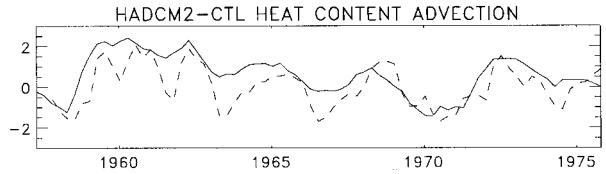

FIG. 13. The equatorial Pacific basin mean meridional temperature advection [rhs of Eq. (1), solid line] and the corresponding $D20$ [lhs of Eq. (1), dashed line] computed from HadCM2-CTL for 20 yr from 1957. Both curves have been normalized by their standard deviations for ease of comparison.

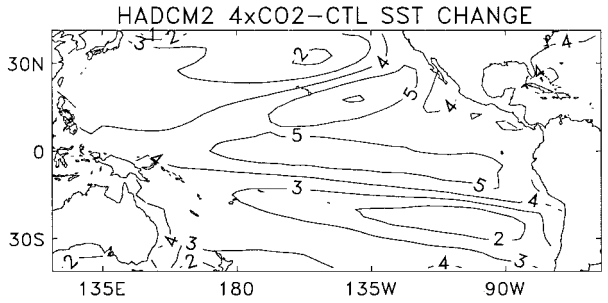

FIG. 14. The SST response to a $4\times CO_2$ increase. The field is obtained by subtracting the HadCM2 control SST field from the $4\times CO_2$ experiment SST field.

months indicating a timescale for the zonally symmetric slow ocean mode of approximately $2\pi \times 10.5$ months ~ 5 yr.

Viewing the mixed SST–ocean dynamics mode in a simplistic way, we can say that the east–west slope of the thermocline adjusts instantaneously to variations in applied wind stress whereas the basin-wide depth of the thermocline undergoes a slow oscillation that determines the main amplitude and frequency charateristics of ENSO. Understanding this zonal mean thermocline depth oscillation is the key to unlocking the mechanisim for ENSO.

Recent work by Jin (1997) and Li (1997) describes the zonal mean thermocline depth oscillation in terms of a transport of mass in and out of the thermocline region and describe an ''ocean recharge paradigm'' for ENSO. The Sverdrup relationship states that the meridional velocity in the thermocline region is proportional to the curl of the surface wind stress. Relating this relationship to the temperature structure of the ocean we see that during periods of strengthend trade winds (La Niña), there is increased Sverdrup transport into the thermocline region and consequently there is a buildup of equatorial heat content that deepens the thermocline depth over the entire equatorial Pacific basin. Correspondingly, during periods of reduced trade winds (El Niño), there is a discharge of heat content that raises the thermocline. Thus, in some volume of ocean centered on the equator, the depth of the zonal mean thermocline will be proportional to the integral over time of the thermal advection in and out of the thermocline region; that is,

$$[D20] \sim -\int \left[v \frac{\partial T}{\partial y} \right] dt, \qquad (1)$$

where $[D20]$ is the zonal mean depth of the 20°C isotherm and $[v(\partial T/\partial y)]$ is the zonally averaged meridional advection of temperature above the 20°C isotherm. Figure 13 shows a plot of both the left-hand side (dashed line) and the right-hand side (solid line) of Eq. (1) from the HadCM2 control run. There is a clear correlation between the two curves on ENSO timescales (the correlation coefficient is 0.7) and thus we deduce that the ocean recharge paradigm is a valid mechanism for the ENSO in the coupled model.

6. Mechanisms for ENSO change at $4\times CO_2$

In the previous section we identified the mechanism for the ENSO signal in the control run of HadCM2 to be a mixed SST–ocean dynamics mode where the ocean dynamics part can be explained in terms of the ocean recharge paradigm of Jin (1997). In this section we explain how this mechanism is modified by increases in greenhouse gases in order to explain the changes in ENSO behavior found in section 4.

To recap, the changes in ENSO at $4\times CO_2$, when compared to the control integration, were as follows: A significant increase in the amplitude of ENSO, a doubling of the frequency of ENSO, and a change in the phase locking of ENSO to the seasonal cycle.

To explain these changes we must first examine the changes in mean climate in the model from control to $4\times CO_2$. Figure 14 shows the difference in SST between the two experiments in the low-latitude Pacific region, that is, the response of the model to a fourfold increase in CO_2 concentrations. The warming over the ocean is far from uniform. The maximum warming occurs at the equator in the central Pacific and to the north in a band orientated toward the northeast. Off the equator, in both hemispheres, there are minima in warming. There is a general picture of not only an increases in mean temperature, but also an increase in the meridional gradient of temperature with the maximium warming occurring on the equator and lesser warming northward and southward. This pattern of warming is likely to be caused by an increase in long-wave cloud feedback associated with an elevation of the high cloud near the equator in the model (Mitchell et al. 1998; Senior and Mitchell 1993).

There are also changes to ocean temperatures below the surface. Shown in Fig. 15 are the subsurface ocean temperatures from the control and from the $4\times CO_2$ experiment. The ocean warming is greater at the surface than it is at depth and this leads to increased vertical temperature gradients. The control experiment (Fig. 15a) has a rather weak thermocline struture, whereas the $4\times CO_2$ experiment (Fig. 15b) has a more well-defined region of strong vertical gradients and also has a generally shallower thermocline. These differences are

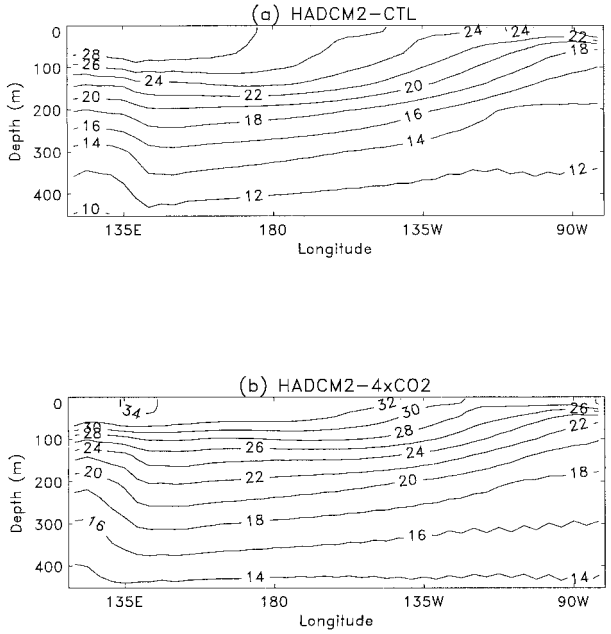

FIG. 15. The subsurface ocean temperature from (a) the HadCM2 control run and from (b) the HadCM2 $4\times CO_2$ run.

especially clear in the region of maximum variability in the central to east of the ocean basin.

How might these changes in SST effect the model ENSO? Timmermann et al. (1999b) speculate that a strengthening of the thermocline leads to enhanced ENSO variability via an increase in the oceanic sensitivity to wind stress anomalies; that is, for a prescribed wind stress anomaly, there will be a greater SST anomaly when the thermocline is sharper. In terms of the ocean recharge paradigm (Jin 1997, and see above) it is the zonally asymmetric part of the oscillation that determines the amplitude of the SST anomalies. The tilting of a rather weak thermocline leads to relatively smaller SST anomalies when compared to the same tilting of a stronger thermocline, a result borne out by simple models of ENSO (e.g., Tziperman et al. 1994). Calculating the oceanic and atmospheric sensitivities as in Timmermann et al. (1999b) by computing the ratios of the covariance of SST and zonal wind stress to the variance of zonal wind stress and SST respectively, we find, as they do, a significant increase in the oceanic sensitivity from control to $4\times CO_2$ but no corresponding increase in the atmospheric sensitivitiy (see Table 2). It is likely that an increase in the vertical gradient of temperature in the thermocline region is responsible for the increase in the amplitude of ENSO in both HadCM2 and in the model of Timmermann et al. (1999b).

The strengthend thermocline may be responsible for an increase in amplitude, but this would have no effect on the timescale of the oscillation. Recall Eq. (1) and the ocean recharge paradigm. The rate at which the thermocline charges and discharges heat content controls the timescale of ENSO [see Jin 1997, Eq. (3.3)]. Slow

TABLE 2. Atmospheric and oceanic sensitivities, defined as the ratio of the covariance of SST in the Niño-3 region and zonal wind stress in the central Pacific to the variance of SST and zonal wind stress, respectively, for the HadCM2 control run and the $4\times CO_2$ run.

	Atmospheric (Pa K^{-1})	Oceanic (K Pa^{-1})
Control	0.0094	31
$4\times CO_2$	0.010	44

rates of charging will give long timescale ENSOs, whereas rapid charging will give faster growing ENSOs and hence a cycle with a shorter period. A crucial parameter in the charging rate will be the meridional temperature gradient within the thermocline [see rhs of Eq. (1)]. Decreasing this gradient will reduce the charging rate, while increasing it will lead to more rapid (or efficient) charging and discharging of the thermocline and a shorter-period ENSO. We may hypothesize that the increased meridional temperature gradient in the vicinity of the equator in Fig. 14 may be responsible for the reduced ENSO frequency found in the $4\times CO_2$ experiment.

In order to test the above hypotheses, that the strengthening of the thermocline leads to a larger amplitude ENSO, and that an increase in the meridional temperature gradient would lead to an increase in the frequency of ENSO, we performed a further experiment with HadCM2. In the experiment, we modified the flux correction field in the control experiment to increase the meridional temperature gradient on either side of the equator and to strengthen the thermocline below the surface. The modification to the flux correction field is shown in Fig. 16 and is included in addition to the existing flux correction field, which keeps the model climate stable. This experiment isolates the effects of the changes in the mean ocean state in the equatorial Pacific, thus excluding all other changes to the climate that occur in the $4\times CO_2$ experiment, such as the warming over land and in other ocean basins, that may effect the ENSO behavior. We note however that althought our forcing field is local to the tropical Pacific, in the $4\times CO_2$ experiment the changes in the mean climate of the re-

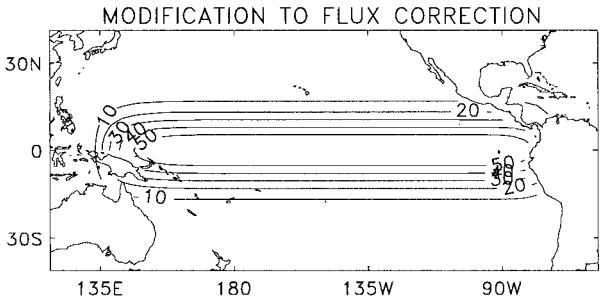

FIG. 16. The modification to the flux correction field used in the experiment to isolate the mechanisms for ENSO changes due to increases in CO_2.

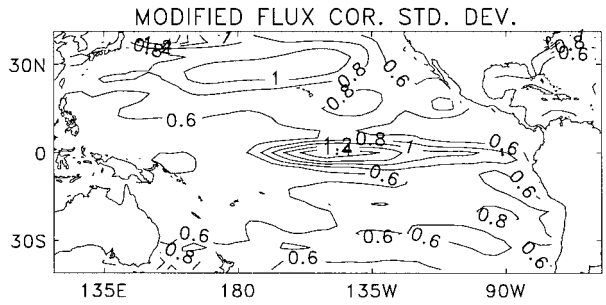

FIG. 17. The standard deviation of SST from the experiment with the modified flux correction field.

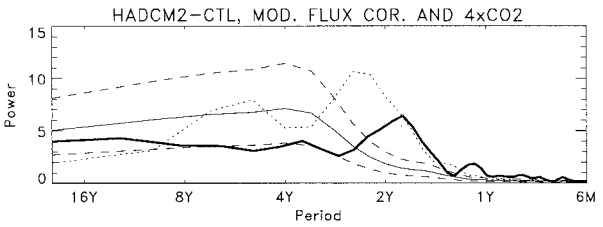

FIG. 18. Power spectra of the Niño-3 indices from the experiment with the modified flux corrrection field (thick black line), the HadCM2 control (thin black line), and the $4\times CO_2$ experiment (dotted line). The thin dashed lines indicate the 95% interval for the power spectra from the control.

gion may be a consequence of other remote changes in climate and not just simply a response to the local forcing.

The standard deviation of SST from the 50 yr of this model run with the modified flux correction field is shown in Fig. 17. This should be compared to the control run standard deviation, which is shown in Fig. 2a. There is an increase in the magnitude of the SST variability in the modified flux corrected run in the central Pacific that is similar to that seen in the $4\times CO_2$ run (not shown), although the increase is not as large as in the $4\times CO_2$ case. The structure of the ocean temperatures below the surface is similar in the modified flux correction run to that in the $4\times CO_2$ run and we conclude that the strengthening of the thermocline is responsible for the increase in amplitude of ENSO.

The power spectra of the Niño-3 series from the experiment with the modified flux correction field is shown in Fig. 18, with the range of variability of the control shown by the dashed lines. The increase in frequency of the ENSO signal is statistically different from the control and is similar to that seen in the $4\times CO_2$ experiment (dotted line). Thus we conclude that it is the change in meridional temperature gradient that is responsible for the shortening of the timescale of ENSO in the $4\times CO_2$ experiment via more rapid charging and discharging of thermocline heat content during the ENSO cycle. In fact, the peak in Fig. 18 is at a somewhat shorter period than the peak for the $4\times CO_2$ run, so it appears that the modification to the flux correction was too extreme in its forcing of the changes in meridional temperature gradients and produced an ENSO with an even shorter period than in the $4\times CO_2$ case.

We have explained the increase in the amplitude of ENSO and the increase in the frequency of ENSO in the coupled model; however, it is not clear why the phase locking of ENSO to the seasonal cycle should change as greenhouse gases increase (see Figs. 5 and 8). Figure 19 shows the monthly standard devation of the Niño-3 index from the experiment with modified flux correction. The ENSO in this run phase locks to the annual cycle in a very similar way to the $4\times CO_2$ run (see Fig. 8) with events occurring more frequently during late Northern Hemisphere summer/early autumn rather than during winter, as in the case of the control run and the observations (Fig. 5). Hence this run, with a simple modification to the flux correction captures the complicated interaction between the seasonal cycle and ENSO. It is hard to understand this result, especially when one considers that there is a lack of a theoretical framework in which to understand why ENSO locks to the annual cycle in the first place. Hence we merely state the result here and leave an explanation for future research.

7. Conclusions and discussion

We have examined the characteristics of the El Niño–Southern Oscillation in the second Hadley Centre Coupled model in climate simulations using preindustrial (control) greenhouse gas concentrations and in simulations with increased levels of greenhouse gases. In the control simulation, the amplitude, spectral characteristics, and phase locking to the annual cycle are well

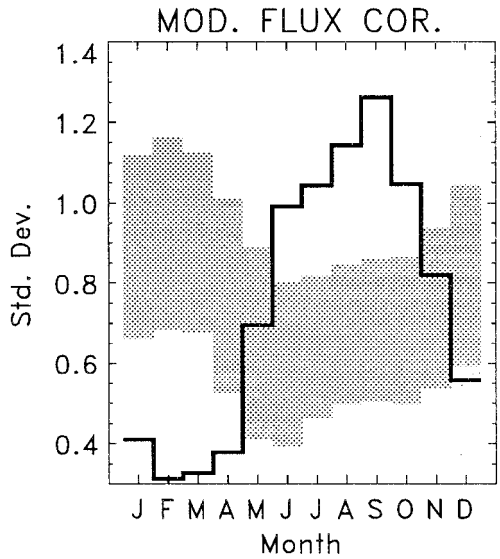

FIG. 19. Standard devations of the Niño-3 anomaly partitioned by month for the experiment with modified flux correction. Values outside the gray-shaded area are statistically different from the HadCM2 control run at the 5% level.

simulated by the model. When levels of greenhouse gases are increased, there are no statisically significant changes in ENSO characteristics until concentrations approach four times preindustrial (equivalent) CO_2. At $4\times CO_2$ there are significant changes in ENSO behavior, with a ~20% increase in the amplitude, a halving of the period of ENSO (implying more El Niño and La Niña events), and a shift in the phase locking of ENSO to the annual cycle with events occurring more frequently during late northern summer/early autumn rather than during northern winter.

The mechanism for the ENSO variability in HadCM2 was identified as a mixed SST–ocean dynamics mode (see, e.g., Neelin et al. 1998) whereby the east–west thermocline slope can be thought to be in equilibrium with the wind stress, while the zonal mean thermocline depth undergoes a slow oscillation that is controlled via the ocean recharge paradigm of Jin (1997). The whole thermocline can be thought of as cyclically charging and discharging heat content and providing the ''memory'' of the cycle and thus determining the slow interannual timescale of ENSO.

The increase in the amplitude of ENSO seen in the $4\times CO_2$ experiment can be explained by an increase in the vertical temperatures gradients in the thermocline region, which are a consequence of the models mean climate response to global warming. The doubling of the frequency of ENSO seen in the model at $4\times CO_2$ can be explained in terms of an increase in the rate of heat content charging and discharging via an increase in meridional temperature gradient on either side of the equator. These hypotheses were confirmed by rerunning a portion of the control simulation with a modified flux correction field in order to simulate the response of the model to increased greenhouse gases. This sensitivity test also showed a change in the phase locking of ENSO to the annual cycle as was the case in the $4\times CO_2$ run.

These results by no means provide a comprehensive and accurate forecast of ENSO behavior in future climates. Not only are there uncertainties in the future concentrations of greenhouse gases, but there are uncertainties in the simulation of ENSO by HadCM2 and in the models mean climate response to increases in greenhouse gases. However, we feel that this study is useful as it points to a possible mechanism for changes in ENSO in future climates via a change in the vertical and meridional thermocline temperature gradients. This study should also be taken in context with other studies on future ENSO changes that all show rather different results (e.g., Meehl et al. 1993; Tett 1995; Knutson et al. 1997; Timmermann et al. 1999b).

Acknowledgments. Many thanks go to Simon Tett and John Mitchell who provided support during this study. The work was supported by U.K. Department of the Environment, Transport and the Regions (PECP/7/12/37), and by the Public Meteorological Service Research and Development Programme.

REFERENCES

Bacher, A., J. M. Oberhuber, and E. Roeckner, 1998: ENSO dynamics and seasonal cycle in the tropical Pacific as simulated by the ECHAM4/OPYC3 coupled general circulation model. *Climate Dyn.,* **14,** 431–450.

Bjerknes, J., 1969: Atmospheric teleconections from the equatorial Pacific. *Mon. Wea. Rev.,* **97,** 163–172.

Cane, M., A. Clement, A. Kaplan, Y. Kushnir, D. Pozdnyakov, R. Seager, S. Zebiak, and R. Murtugudde, 1997: Twentieth-century sea surface temperature trends. *Science,* **275,** 957–960.

Chatfield, C., 1984: *The Analysis of Time Series.* 3d ed. Chapman and Hall, 241 pp.

Cox, M. D., 1984: A primitive equation, three dimensional model of the ocean. Ocean Group Tech. Rep. 1, 141 pp. [Available from Geophysical Fluid Dynamics Laboratory/NOAA, P.O. Box 308, Princeton, NJ 08542.]

Cullen, M. J. P., 1993: The unified forecast/climate model. *Meteor. Mag.,* **122,** 81–94.

Gillett, N. P., M. R. Allen, and S. F. B. Tett, 2000: Modelled and observed variability in atmospheric verical temperature structure. *Climate Dyn.,* **12,** 49–61.

Hasselmann, K., 1993: Optimal fingerprints for the detection of time dependent climate change. *J. Climate,* **6,** 1957–1971.

Hegerl, G., K. Hasselmann, U. Cubasch, J. Mitchell, E. Roeckner, R. Voss, and J. Waszkewitz, 1997: Multi-fingerprint detection and attribution analysis of greenhouse gas, greenhouse gas-plus-aerosol and solar forced climate change. *Climate Dyn.,* **13,** 613–634.

Houghton, J. T., L. G. M. Filho, B. A. Callander, N. Harris, A. Kattenberg, and K. M., Eds., 1995: *Climate Change 1995.* Cambridge University Press, 572 pp.

Jiang, N., J. D. Neelin, and M. Ghil, 1995: Quasi-quadrennial and quasi-biennial variability in the equatorial Pacific. *Climate Dyn.,* **12,** 101–112.

Jin, F.-F., 1997: An equatorial ocean recharge paradigm for ENSO. Part I: Conceptual model. *J. Atmos. Sci.,* **54,** 811–829.

——, and J. D. Neelin, 1993: Modes of interannual tropical ocean–atmosphere interaction—A unified view. Part I: Numerical results. *J. Atmos. Sci,* **50,** 3477–3503.

——, ——, and M. Ghil, 1994: El Niño on the devil's staircase: Annual subharmonic steps to chaos. *Science,* **264,** 70–72.

Johns, T. C., R. E. Carnell, J. F. Crossley, J. M. Gregory, J. F. B. Mitchell, C. A. Senior, S. F. B. Tett, and R. A. Wood, 1997: The second Hadley Centre coupled ocean–atmosphere GCM: Model description, spinup and validation. *Climate Dyn.,* **13,** 103–134.

Kiehl, J. T., 1998: Simulation of the tropical warm pool with the NCAR Climate System Model. *J. Climate,* **11,** 1342–1355.

Knutson, T. R., and S. Manabe, 1998: Model assessment of decadal variability and trends in the tropical Pacific. *J. Climate,* **11,** 2273–2296.

——, ——, and D. Gu, 1997: Simulated ENSO in a global coupled ocean–atmosphere model: Multidecadal amplitude modulation and CO_2 sensitivity. *J. Climate,* **10,** 42–63.

Levitus, S., 1982: *Climatological Atlas of the World Ocean.* NOAA Prof. Paper 13, U.S. Government Printing Office, 173 pp.

Li, T., 1997: Phase transition of the El Niño–Southern Oscillation: A stationary SST mode. *J. Atmos. Sci.,* **54,** 2872–2887.

Meehl, G. A., and W. M. Washington, 1996: El Niño-like climate change in a model with increased atmospheric CO_2 concentrations. *Nature,* **382,** 56–60.

——, and J. M. Arblaster, 1998: The Asian–Australian monsoon and El Niño–Southern Oscillation in the NCAR Climate System Model. *J. Climate,* **11,** 1356–1385.

——, G. W. Branstator, and W. M. Washington, 1993: Tropical Pacific interannual variability and CO_2 climate change. *J. Climate,* **6,** 42–63.

Mitchell, J. F. B., and T. C. Johns, 1997: On the modification of global warming by sulfate aerosols. *J. Climate,* **10,** 245–267.

——, ——, J. M. Gregory, and S. F. B. Tett, 1995: Climate response

to increasing levels of greenhouse gases and sulphate aerosols. *Nature,* **376,** 501–504.

——, ——, and C. A. Senior, 1998: Transient response to increased greenhouse gases using models with and without flux adjustment. Hadley Centre Tech. Note No. 2, 35 pp. [Available from Hadley Centre, U.K. Meteorological Office, London Road, Bracknell, Berkshire, RG12 2SZ, United Kingdom.]

Neelin, J. D., and F.-F. Jin, 1993a: Modes of interannual tropical ocean–atmosphere interaction—A unified view. Part II: Analytical results in the weak-coupling limit. *J. Atmos. Sci.,* **50,** 3504–3522.

——, and ——, 1993b: Modes of interannual tropical ocean–atmosphere interaction—A unified view. Part III: Analytical results in fully coupled cases. *J. Atmos. Sci,* **50,** 3523–3540.

——, and Coauthors, 1992: Tropical air–sea interaction in general circulation models. *Climate Dyn.,* **7,** 73–104.

——, D. S. Battisti, A. C. Hirst, F.-F. Jin, Y. Wakata, T. Yamagata, and S. E. Zebiak, 1998: ENSO theory. *J. Geophys. Res.,* **103** (C7), 14 261–14 290.

Philander, S. G., 1990: *El Niño, La Niña, and the Southern Oscillation.* International Geophysics Series, Vol. 46, Academic Press, 293 pp.

Rajagopalan, B., U. Lall, and M. Cane, 1997: Anomalous ENSO occurances: An alternate view. *J. Climate,* **10,** 2351–2357.

Rayner, N., E. B. Horton, D. E. Parker, C. K. Folland, and R. B. Hackett, 1996: Version 2.2 of the global sea-ice and sea surface temperature data set 1903–1994. Climate Research Tech Note No. 74, 29 pp. [Available from Hadley Center, U.K. Meteorological Office, London Road, Bracknell, Berkshire, RG12 2SZ, United Kingdom.]

Schneider, E. K., B. Huang, and J. Shukla, 1995: Ocean wave dynamics and El Niño. *J. Climate,* **8,** 2415–2439.

Senior, C. A., and J. F. B. Mitchell, 1993: Carbon dioxide and climate: The impact of cloud parameterization. *J. Climate,* **6,** 393–418.

Suarez, M. J., and P. S. Schopf, 1988: A delayed action oscillator for ENSO. *J. Atmos. Sci.,* **45,** 3283–3287.

Tett, S. F. B., 1995: Simulation of El Niño–Southern Oscillation-like variabilility in a global AOGCM and its response to CO_2 increase. *J. Climate,* **8,** 1473–1502.

——, J. F. B. Mitchell, D. E. Parker, and M. R. Allen, 1996: Human influence on the atmospheric vertical temperature structure: Detection and observations. *Science,* **247,** 1170–1173.

——, T. C. Johns, and J. F. B. Mitchell, 1997: Global and regional variability in a coupled AOGCM. *Climate Dyn.,* **13,** 303–323.

Timmermann, A., 1999: Detecting the nonstationary response of ENSO to greenhouse warming. *J. Atmos. Sci.,* **56,** 2313–2325.

——, M. Latif, A. Grotzner, and R. Voss, 1999a: Modes of climate variability as simulated by the coupled atmosphere–ocean model ECHAM3/LSG, Part I: ENSO-like climate variability and its low-frequency modulation. *Climate Dyn.,* **15,** 605–618.

——, J. Oberhuber, A. Bacher, M. Esch, M. Latif, and E. Roeckner, 1999b: Increased El-Niño frequency in a climate model forced by future greenhouse warming. *Nature,* **398,** 694–696.

Torrence, C., and G. P. Compo, 1998: A practical guide to wavelet analysis. *Bull. Amer. Meteor. Soc.,* **79,** 61–78.

Trenberth, K., and T. Hoar, 1996: The 1990–1995 El-Niño–Southern Oscillation event: Longest on record? *Geophys. Res. Lett.,* **23,** 57–60.

Tziperman, E., L. Stone, M. A. Cane, and H. Jarosh, 1994: El-Niño chaos: Overlapping of resonances between the seasonal cycle and the Pacific Ocean–atmosphere oscillator. *Science,* **264,** 72–74.

Wunsch, C., 1999: The interpretation of short climate records, with comments on the North Atlantic and Southern Oscillations. *Bull. Amer. Meteor. Soc.,* **80,** 245–255.